Aqueous Li-ion Battery Enabled by Halogen Conversion-Intercalation Chemistry in Graphite

Chongyin Yang[1,7], Ji Chen[1,7], Xiao Ji[1], Travis P. Pollard[2], Xujie Lü[3], Cheng-Jun Sun[4], Singyuk Hou[1], Qi Liu[4,5], Cunming Liu[4], Tingting Qing[1], Yingqi Wang[3], Oleg Borodin[2], Yang Ren[4], Kang Xu[2] & Chunsheng Wang[1,6,*]

[1]Department of Chemical and Biomolecular Engineering, University of Maryland, College Park, USA

[2]Electrochemistry Branch, Power and Energy Division, Sensor and Electron Devices Directorate, U.S. Army Research Laboratory, Adelphi, USA

[3]Center for High Pressure Science and Technology Advanced Research, Shanghai, China

[4]X-ray Science Division, Advanced Photon Source, Argonne National Laboratory, Argonne, USA

[5]Department of Physics, City University of Hong Kong, Hong Kong, China

[6]Department of Chemistry and Biochemistry, University of Maryland, College Park, USA

[7]These authors contributed equally to this work.

[*]E-mail: cswang@umd.edu

Recent advances in aqueous lithium batteries via a "water-in-salt electrolyte" approach have significantly expanded their electrochemical window to 3.0–4.0 V, making it possible to couple high voltage cathodes with low-potential graphite anodes[1-4]. However, the limited lithium intercalation capacities (< 200 mAh g^{-1}) of typical transition metal oxide cathodes[5,6] preclude higher energy densities, although partial[7,8] or exclusive[9] anionic redox reactions (O/O^{2-}, S/S^{2-}, *etc.*) promise higher capacity at the expense of reversibility. Here we report a new halogen conversion-intercalation chemistry in graphite that resolves the dilemma, delivering a capacity of 243 mAh g^{-1} (total weight of composite electrode) at an average potential of 4.2 volt versus Li/Li^+. Experimental characterization and modeling attribute this high specific capacity to a densely-packed stage one graphite-intercalation-compound (GIC) $C_{3.5}[Br_{0.5}Cl_{0.5}]$, which can reversibly form in water-in-bisalt electrolyte (WiBS). Coupling this cathode chemistry with a protected graphite anode, a 4.0 V class aqueous Li-ion full cell delivers an energy density of 460 Wh/(kg of total composite electrode) with

~100% coulombic efficiency. This anion intercalation-conversion mechanism offers a post-lithium ion concept that integrates high energy densities of conversion reactions, excellent reversibility of intercalation mechanism, and improved safety of aqueous nature.

Leveraging the anionic-redox reaction of halide anions (Br^- and Cl^-) in graphite, a composite electrode containing equimolar lithium halide salts $(LiBr)_{0.5}(LiCl)_{0.5}$-graphite, (hereafter denoted as LBC-G), was synthesized by mixing anhydrous LiBr and LiCl with graphite at an optimal mass ratio of 2:1:2 (corresponding to molar ratio of $(LiBr)_{0.5}(LiCl)_{0.5}C_{3.7}$, see Methods). Herein, the highly concentrated WiBS electrolyte confined partially hydrated LiBr/LiCl within the solid cathode matrix, while upon oxidation, Br^0 and Cl^0 are stabilized by their sequential intercalation into graphite host as solid GICs. This new cathode chemistry inherits the high energy of conversion-reaction and the excellent reversibility from topotactic intercalation, and fundamentally differ from the 'dual-ion' batteries that reversibly intercalate complex anions (PF_6^-, BF_4^-, $TFSI^-$) into graphite at low density packing, where these stable anions do not experience redox reactions, resulting in low capacities below 120 mAh g^{-1}.[10,11]

Upon exposure to WiBS electrolyte, the anhydrous LiBr/LiCl extract approximate 2.4% water in WiBS (Extended Data Fig. 1a) forming a hydrated LiBr/LiCl layer on LBC-G surface (schematically illustrated in Figure 1a, estimated overall formulations of hydrated salts: $LiBr{\cdot}0.34H_2O$-$LiCl{\cdot}0.34H_2O$, electrode/electrolyte = 1:20), which accelerates the halogens redox reaction in the form of liquefied anions. Due to the immiscibility of halide anions in WiBS, this hydrated layer is thermodynamically phase-separated from the bulk electrolyte and builds dynamic water equilibrium (Extended Data Fig. 1c), as previously observed for lithium polysulfides[4]. Such a liquefied layer allows for Li^+ transport but confines all the halide anions within the cathode, as evidenced by both MD simulation (Extended Data Fig. 1e) and the extreme low Cl/Br content (<32 ppm) detected by chromatographic analysis in WiBS equilibrated with LiCl/LiBr solution for 500 hours (Extended Data Fig. 1d).

The electrochemical behaviors of LBC-G were firstly evaluated in a three-electrode cell with an aqueous gel polymer electrolyte based on WiBS (see Methods). The cyclic voltammetry (Figure 1b) and charge/discharge profiles (Figure 1c-d) indicated two distinct reactions: 4.0–4.2 V for Br^--intercalation and 4.2–4.5 V for Cl^--intercalation, respectively, which deliver a highly reversible discharge capacity of 243 mAh g^{-1} (of the total mass of LBC-G composite), 82% of

which is retained over 230 cycles at a coulombic efficiency (CE%) of 100 % after the 80th cycle at a current density of 80 mA g^{-1} (0.2 C). The two-step redox reactions correspond to (Figure 1a):

$$LiBr + C_n \leftrightarrow C_n[Br] + Li^+ + e^- \qquad 4.0 - 4.2\ V \qquad (1)$$

$$LiCl + C_n[Br] \leftrightarrow C_n[BrCl] + Li^+ + e^- \qquad 4.2 - 4.5\ V \qquad (2)$$

where *n* is the molar ratio of carbon atoms to the intercalated halogens in the GIC. Upon charging, Br^- is the first species within the hydration layer to oxidize to a near-zero state (Br^0) and intercalates into graphite, forming $C_n[Br]$ (eq. 1). Further charging oxidizes and intercalates Cl^- (eq. 2), forming a mixed intercalation compound $C_n[BrCl]$. The oxidation of each halogen involves one-electron transfer reaction (theoretical capacity: 309 mAh g^{-1} for LiBr, 632 mAh g^{-1} for LiCl)[12], and the release of one Li^+ into the bulk electrolyte. Upon discharging, the reverse process occurs: Cl^0 and Br^0 successively de-intercalate from graphite-interlayer, reduce into halides, and recombine with Li^+ to form both solid LiCl/LiBr crystals and liquefied halides outside of the graphite-interlayer (Extended Data Fig. 2a-d). WiBS plays another essential role in this chemistry by pushing the oxidation potential of water to ~4.9 V vs. Li/Li^+,[3] realizing full reversibility of the halide oxidation/reduction without electrolyte decomposition (Extended Data Fig. 3).

Galvanostatic intermittent titration technique (GITT) was used to examine the quasi-equilibrium potentials and kinetics of reactions at different stages. The quasi-equilibrium potentials are ~4.05 V for Br^- and ~4.35 V for Cl^- oxidation/intercalation, respectively (Figure 1e), while the total diffusion coefficients were estimated between 10^{-15}–10^{-13} $cm^2\ s^{-1}$ (red and blue curves in Figure 1e inset). The diffusion coefficients were also estimated with electrochemical impedance spectroscopy (EIS, Figure 1f), whose fitting with the equivalent circuit (Extended Data Fig. 4a) yields the apparent ionic diffusion coefficients to be 6.85×10^{-15}–2.07×10^{-14} $cm^2\ s^{-1}$ (green circles in Figure 1e inset), in excellent agreement with GITT. Considering the extremely high diffusion coefficients of halogens in graphite-interlayer[13] (EIS independence with graphite size in Extended Data Fig. 4b), the mass transfer of Br^- and Cl^- between solid salts and graphite surface constitutes the rate-determining step in this chemistry.

Figure 1g compared gravimetric energy densities of LBC-G composite with state-of-the-art cathode materials. LBC-G provides a practical gravimetric capacity of 231 mAh g^{-1} (of total

weight of electrode) and volumetric capacity of 450 mAh mL^{-1} (of total volume of electrode) at an average discharge voltage of 4.2 V, yielding an unprecedented energy density of 970 Wh kg^{-1} that is almost twice as much as transition-metal intercalation cathodes. Although sulfur conversion chemistry provides comparable gravimetric energy density, LBC-G is far superior per volume due to its compacter storage of halogens in graphite interlayer (Extended Data Fig. 4c).

In situ Raman spectroscopy (100–550 cm^{-1}) was performed to probe the intercalation mechanism of halogen into graphite (Figure 2a). With the states-of-charge (SOC) at 0%–50%, a characteristic peak (ω_0 = 242 cm^{-1}) was detected, which corresponds to stretch-mode of intercalated Br_2[14]. Further charging introduced a feature corresponding to BrCl-intercalant (ω_0 = 310 cm^{-1}), verified by a reference prepared via chemical intercalation of BrCl into graphite (Extended Data Fig. 6g). The peak intensity of BrCl-intercalant increases with charging of LBC-G to 4.5 V. The interaction with graphene layer weakens the interatomic bonds of halogen-intercalants, causing the frequency downshift from 318 cm^{-1} for free Br_2 (liquid) to 242 cm^{-1} for Br_2-intercalant, and from 427 cm^{-1} for free BrCl (gaseous) to 310 cm^{-1} for BrCl-intercalant[15,16]. We note that during charging/discharging between 3.2 V and 4.5 V, no free Br_2 or BrCl peaks were detected, until we deliberately destabilized the fully intercalated BrCl-GIC with a high-intensity laser beam (red curve, Figure 2a), suggesting that all the halogens are intercalated into graphite structure rather than absorbing on its surface. Upon discharging, the original Raman spectra were restored demonstrating the reversibility of LCC-G chemistry.

Ex situ X-ray absorption near edge structure (XANES) spectra reveals how the redox reaction sequence of halogens occurs in LBC-G cathode (Figure 2b). For Br *K*-edge, a distinct and sharp peak at ~13,473 eV, attributed to the Br intra-atomic $1s \rightarrow 4p$ transition, appeared immediately upon charging. The intensity of this peak, reflecting the hole-density on Br 4*p*-orbitals, gradually increases accompanied by the blue-shifted absorption edge ($1s \rightarrow p$ continuum, ~13,480 eV)[17]. It presents clear evidence that Br^- accepts the hole to be oxidized to Br^0. For Cl K-edge (Figure 2c), only single absorption edge ($1s \rightarrow$continuum) at ~2,822 eV was observed at the first charge plateau (SOC 0% – 50%), indicating that all Cl remained as Cl^-[18]. Cl^--oxidation occurs only at the second charge plateau (SOC 50%–100%) as demonstrated by the appearance of Cl intra-atomic $1s \rightarrow 3p$ transition peak (~2,821 eV) due to the hole taken by Cl^-. By comparison with the reference spectra (dash lines in Fig. 2b) of chemically intercalated Br_2-GIC

and liquid Br_2, apparently Br was mostly oxidized, but has not entirely reached Br^0 at the first charge plateau (SOC 0% – 50%). Both DFT simulations (Figure 2d) and literature[19] suggest that Br remain at approximately -0.16 in Br_2-GICs at 50% SOC. Only after the subsequently intercalated Cl tends to associate with Br intercalated earlier would the Br-oxidation state further increase to nearly Br^0 (-0.05) due to its relatively lower electron-negativity than Cl. The oxidation state of Cl becomes -0.25.

Additional evidence supporting this conversion-intercalation mechanism comes from the charge/discharge profiles of LBC-G at different LiBr/LiCl molar ratios (Figure 2e-f). The capacity ratios of two charge/discharge plateaus are highly correlated with LiBr/LiCl molar ratio. The specific capacities calculated by the weights of LiBr in the LBC-G cathodes in the low-potential plateau (< 4.25 V, Figure 2e and Extended Data Figure 5a) at a low rate of ≤ 0.2C is very close to the theoretical redox capacity of LiBr (309 mAh/g), while that of the high-potential charging plateaus (> 4.25 V), when calculated on the weights of LiCl, is close to the theoretical redox capacity of LiCl (632 mAh/g, Figure 2f). Interestingly, CE% of LBC-G cathodes in the high-voltage plateau increase with increasing of LiBr/LiCl ratio, implying that the solo intercalation of Cl^0 in graphite is thermodynamically forbidden at room temperature[20], unless it is paired with a Br^0. In sharp contrast, neat $(LiBr)_{0.5}(LiCl)_{0.5}$ in absence of graphite could deliver a high oxidation capacity during the initial charging, but the discharge capacity is very low due to the loss of gaseous halogens (Extended Data Figure 5b). Carbon host can improve the reversibility by adsorbing halogens on surface (Extended Data Figure 5c), while CE% improves with their graphitization degree (Extended Data Figure 5d-h), suggesting graphitic materials provide a host structure that can reversibly accommodate the halogen oxidation products.

The structural evolution of graphite super-lattice is revealed by *in situ* Raman spectroscopy (1200–2850 cm^{-1}) during halogen-intercalation (Figure 3a)[21]. Upon halogen-intercalation, the graphite G band (1,584 cm^{-1}) diminishes and gradually evolves into a feature corresponding to stages II GIC structure at 50% SOC, while at 100% SOC peak further shifts to 1,631 cm^{-1}, indicating a stages I GIC structure[22,23]. Upon discharging, a fully reversible change in Raman spectra is observed. A more detailed evolution in the staging structure was revealed by *ex situ* X-ray diffraction (XRD) spectra. LBC-G cathode (reflection geometry, Figure 3b) shows shifting dominant peak of (*0 0 m+1*) and subdominant peak of (*0 0 2m+2*) during halogen

intercalation/de-intercalation, verified by the reference patterns (Extended Data Figure 6 a–f) and literature[24]. According to the well-reported intercalant gallery heights (7.00 Å for Br_2 and 6.85 Å for BrCl)[25,26], the accurate *d* spacing with different GIC stage numbers *m* can be calculated (Extended Data Table 1&2, calculation details in Methods). Close examinations suggested a successive progression of *d* spacing for the dominant peak from 3.35 Å for pristine graphite (*0 0 2*), to d_{003} ~3.45 Å for stage II Br_2-GIC between SOC 0%~50%. Since the intercalant gallery height was slightly lower, further intercalation of Cl caused gradual shrink of *d* spacing, eventually reaching stage I BrCl-GIC (d_{002} ~3.43 Å) at 100% SOC. *In situ* XRD of LBC-G (Figure 3c) showed the *d* spacing of (*0 0 m+1*) experienced a continuous shifting during charging, indicating the gradual expansion of graphene-interlayers when accommodating halogens[20]. A complete reversal of the above progression was again observed upon discharging, indicating a full recovery of the graphitic structure in a complete cycle.

The in-plane configuration and coordination of halogen-intercalants in graphite provide critical knowledge to determine the optimum intercalation concentration of this cathode chemistry. Since such structure is independent of overall intercalate concentration, the stoichiometry n of C_n[Br] and C_n[BrCl] always remain the same in each intercalation domain[20]. *Ex situ* high-energy XRD (perpendicular incidence) for LBC-G at 50% and 100% SOCs (Figure 3d) showed multiple asymmetric and overlapping peaks, revealing mild level of long-range ordering of intercalant in-plane configurations. At SOC 50%, only three peaks in low diffraction angles can be indexed according to the single-crystal Br_2-GIC reference[27], indicating multi-phase coexistence, localized disorder, and structure strain. DFT simulations based on two stoichiometries *n* = integer multiples of 7 and 8 (Extended Data Fig. 7) yield zig-zag polymeric-like chains of –Br–Br– or –Br–Cl– with the nearest in-plane distance of 2.4–3.2 Å (Figure 3e-f insets). All these configurations have quite similar potentials (within 20 mV), indicating that the real materials might be slightly disordered due to the coexistence of these idealized model structures[28], in accord with *ex situ* XRD patterns (Figure 3d). Molecular dynamics simulations (Extended Data Fig. 8) predict that close Br–Br contacts may serve as hotspots for interconversion between different phases.

By fitting Br extended X-ray absorption fine structure (EXAFS) of LBC-G at 50% and 100% SOC (Figure 3e-f), the most compatible models were C_{7m}[BrBr] and C_{7m}[BrCl], both with

two sets of the nearest in-plane distances (Br-X1 and Br-X2, X=Br or Cl) instead of consistent distances for C_{8m}[BrBr] and C_{8m}[BrCl] (Extended Data Fig. 9). Due to the interaction with π-electrons of graphene planes, the average nearest in-plane distances of halogen intercalants were 2.50 Å for Br-Br1, 3.15 Å for Br-Br2, 2.43 Å for Br-Cl1 and 3.00 Å for Br-Cl2, somewhat longer than bond lengths in free Br_2 (~2.30 Å) and BrCl (2.18 Å) molecules. However, these nearest in-plane distances are much shorter than those of alkali metal GICs (4.30 – 4.92 Å) and large anions GICs (8 – 10 Å)[29], which means the halogen-intercalates possess one of the highest in-plane densities among all GICs reported. This high-density packing is mainly due to the near-zero oxidation valence of halogen-intercalates, which generates much lower coulomb repulsion from average effective charge ~ −0.16 per halogen atom (Figure 2d), as compared with ~ +0.90 for Li-GIC[30] and −1 for complex anions.

Aqueous LIB full cells were constructed using an aqueous gel electrolyte derived from WiBS[4] and LBC-G cathode coupled with a graphite anode protected by a highly fluorinated ether (HFE) polymer gel[2], which was developed earlier for 4 V aqueous LIB (cell configuration in Extended Data Fig. 4d-e). A stable discharge capacity of 127 mAh/g (total anode/cathode mass) was obtained at an average voltage of 4.1 V at 0.2 C (Figure 4a), and 74% of this initial capacity was retained over 150 cycles at an average CE% of 99.8% (Figure 4b). The low self-discharge rate (Extended Data Fig. 2f) demonstrated that the super-concentrated aqueous gel electrolyte effectively suppressed the parasitic reactions, especially the water decomposition and loss of halogen active material from cathode.

Since formation of hydrated LiBr/LiCl layer via extraction of water from WiBS is critical for high power density, the WiBS/cathode mass ratio affects the rate performance. The rate capability was severely compromised when the electrolyte/electrodes mass ratio was reduced from 4:1 to 1:2 (Figure 4c). However, high WiBS/cathode ratio is not desired either because it will reduce energy density. As a simple solution to this dilemma, the anhydrous salts were replaced by their monohydrate forms ($LiBr{\cdot}H_2O$/$LiCl{\cdot}H_2O$, Extended Data Fig. 1b) resulting in almost identical charge/discharge profiles (Figure 4 a & b). The rate capability of such full cell is much better while the impact of electrolyte/electrodes mass ratio is minimized. Given that battery performances constructed with LiBr/LiCl monohydrates are independent of electrolyte amount, we estimated the energy density of such aqueous LIBs to be around 460 Wh kg^{-1} (total

mass of cathode and anode). This energy density is greater than the state-of-the-art non-aqueous LIBs (Figure 4d). After counting the electrolyte mass, the full cell energy density still reaches up to 304 Wh kg^{-1}. Importantly, this high energy density comes with intrinsic safety and environmental insensitivity brought by its aqueous nature. The proposed conversion-intercalation aqueous cathode chemistry offers an energy-dense concept for future battery that is cost effective, safe, and flexible.

Reference:

1 Suo, L. *et al.* "Water-in-salt" electrolyte enables high-voltage aqueous lithium-ion chemistries. *Science* **350**, 938-943 (2015).

2 Yang, C. *et al.* 4.0 V Aqueous Li-Ion Batteries. *Joule* **1**, 122-132 (2017).

3 Suo, L. *et al.* Advanced High-Voltage Aqueous Lithium-Ion Battery Enabled by "Water-in-Bisalt" Electrolyte. *Angewandte Chemie International Edition* **55**, 7136-7141 (2016).

4 Yang, C. *et al.* Unique aqueous Li-ion/sulfur chemistry with high energy density and reversibility. *Proc Natl Acad Sci U S A* **114**, 6197-6202 (2017).

5 Larcher, D. & Tarascon, J. M. Towards greener and more sustainable batteries for electrical energy storage. *Nature Chemistry* **7**, 19 (2014).

6 Radin, M. D. *et al.* Narrowing the Gap between Theoretical and Practical Capacities in Li-Ion Layered Oxide Cathode Materials. *Advanced Energy Materials* **7**, 1602888-n/a (2017).

7 Zhan, C. *et al.* Enabling the high capacity of lithium-rich anti-fluorite lithium iron oxide by simultaneous anionic and cationic redox. *Nature Energy* **2**, 963-971 (2017).

8 Lee, J. *et al.* Reversible Mn(2+)/Mn(4+) double redox in lithium-excess cathode materials. *Nature* **556**, 185-190 (2018).

9 Bruce, P. G., Freunberger, S. A., Hardwick, L. J. & Tarascon, J. M. Li-O2 and Li-S batteries with high energy storage. *Nat Mater* **11**, 19-29 (2012).

10 Seel, J. A. & Dahn, J. R. Electrochemical Intercalation of PF_6 into Graphite. *Journal of The Electrochemical Society* **147**, 892-898 (2000).

11 Milliken, J. W. & Fischer, J. E. Ionic salt limit in graphite–fluoroarsenate intercalation compounds. *The Journal of Chemical Physics* **78**, 5800-5808 (1983).

12 Wu, F. & Yushin, G. Conversion cathodes for rechargeable lithium and lithium-ion batteries. *Energy Environ. Sci.* **10**, 435-459 (2017).

13 Axdal, S. H. A. & Chung, D. D. L. Kinetics and thermodynamics of intercalation of bromine in graphite—I. Experimental. *Carbon* **25**, 191-210 (1987).

14 Erbil, A., Dresselhaus, G. & Dresselhaus, M. S. Raman scattering as a probe of structural phase transitions in the intercalated graphite-bromine system. *Physical Review B* **25**, 5451-5460 (1982).

15 Anthonsen, J. The Raman Spectra of Some Halogen Gas Hydrates. *Acta Chemica Scandinavica* **29a**, 175-178 (1975).

16 Stammreich, H. & Forneris, R. The Raman Frequency of Bromine Monochloride. *The Journal of Chemical Physics* **21**, 944-945 (1953).

17 Heald, S. M. & Stern, E. A. Extended-x-ray-absorption-fine-structure study of theBr2-graphite system. *Physical Review B* **17**, 4069-4081 (1978).
18 Huggins, F. E. & Huffman, G. P. Chlorine in coal: an XAFS spectroscopic investigation. *Fuel* **74**, 556-569 (1995).
19 Heald, S. M. & Stern, E. A. EXAFS study of Br2-graphite intercalation compounds. *Synthetic Metals* **1**, 249-255 (1980).
20 Selig, H. & Ebert, L. B. Graphite Intercalation Compounds. *Advances in Inorganic Chemistry and Radiochemistry* **23**, 281-327 (1980).
21 Dresselhaus, M. S. & Dresselhaus, G. Intercalation compounds of graphite. *Advances in Physics* **30**, 139-326 (1981).
22 Cao, J. *et al.* Two-Step Electrochemical Intercalation and Oxidation of Graphite for the Mass Production of Graphene Oxide. *Journal of the American Chemical Society* **139**, 17446-17456 (2017).
23 Lin, M. C. *et al.* An ultrafast rechargeable aluminium-ion battery. *Nature* **520**, 325-328 (2015).
24 Leung, S. Y. *et al.* Structural studies of graphite intercalation compounds using (00l) x-ray diffraction. *Physical Review B* **24**, 3505-3518 (1981).
25 Furdin, G., Bach, B. & Herold, A. Contribution à l'étude du système ternaire graphite-brome-chlore. *A., C. R . Acad. Sci., Ser. C* **271**, 683 (1970).
26 Eeles, W. & Turnbull, J. The crystal structure of graphite-bromine compounds. *Proc. R. Soc. Lond. A* **283**, 179-193 (1965).
27 Sasa, T., Takahashi, Y. & Mukaibo, T. Crystal structure of graphite bromine lamellar compounds. *Carbon* **9**, 407-416 (1971).
28 Chung, D. Structure and phase transitions of graphite intercalated with bromine. *Phase Transitions: A Multinational Journal* **8**, 35-57 (1986).
29 Placke, T. *et al.* In situ X-ray Diffraction Studies of Cation and Anion Inter-calation into Graphitic Carbons for Electrochemical Energy Storage Applications. *Zeitschrift für anorganische und allgemeine Chemie* **640**, 1996-2006 (2014).
30 Titantah, J. T., Lamoen, D., Schowalter, M. & Rosenauer, A. Density-functional theory calculations of the electron energy-loss near-edge structure of Li-intercalated graphite. *Carbon* **47**, 2501-2510 (2009).

Acknowledgements The principal investigators (C.W. and K.X.) received the financial support from the US Department of Energy (DOE) ARPA-E Grant DEAR0000389. This research used resources of the Advanced Photon Source, an Office of Science User Facility operated for the U.S. DOE Office of Science by Argonne National Laboratory, and was supported by the U.S. DOE under Contract No. DE-AC02-06CH11357, and the Canadian Light Source and its funding partners.

Author Contributions C.Y. and J.C. contributed equally to this work. C.Y., J.C. and C.W. conceived the idea. C.Y., J.C., S.H. and T.Q. prepared the materials and performed electrochemical experiments. X.J., O.B. and T.P.P. conducted DFT and MD simulations. C.Y.

and J.C. conducted Raman spectroscopy measurements. C.Y., X.L., Q.L. and Y.R. performed X-ray diffraction measurements. C.Y., Y.W., C.L. and C.S. performed X-ray absorption spectroscopy measurements. All the authors discussed the results, analyzed the data and drafted the manuscript.

Competing interests The authors declare no competing interests.

Additional information

Extended data is available for this paper at https://doi.org/10.1038/xxxxx.

Reprints and permissions information is available at https://www.nature.com/reprints.

Correspondence and requests for materials should be addressed to C.W. (cswang@umd.edu).

Publisher's note: Springer Nature remains neutral with regard to jurisdictional claims in published maps and institutional affiliations.

METHODS

Preparation of electrodes. For the three-electrode $(LiBr)_{0.5}(LiCl)_{0.5}$-graphite composite (designated as sample LBC-G) was obtained by homogenously mixing anhydrous LiBr (99.9%, Sigma-Aldrich), LiCl (99.9%, Sigma-Aldrich) and synthetic graphite powder (TIMCAL TIMREX® KS4, average particle size ~ 4.1 μm) by zirconia ball milling for 15 min. The molar ratio of LiBr/LiCl was 1:1, while the mass ratio of LiBr/LiCl/graphite was ~ 2:1:2. In the full cells with LiBr/LiCl monohydrates, all the procedures were the same except replacing anhydrous LiBr/LiCl with $LiBr{\cdot}H_2O$ (99.95%, Sigma-Aldrich) and LiCl (99.95%, Sigma-Aldrich). Other control samples were obtained by adjusting the composites as following mass ratios: LiBr/LiCl/titanium nanopowder ~ 2:1:60 for $(LiBr)_{0.5}(LiCl)_{0.5}$-Ti; LiBr/LiCl/active carbon ~ 2:1:9 for $(LiBr)_{0.5}(LiCl)_{0.5}$-AC; LiBr/LiCl/graphited acetylene black ~ 2:1:9 for $(LiBr)_{0.5}(LiCl)_{0.5}$-CB. Composite LBC-G cathodes were fabricated by compressing LBC-G composite and poly(vinylidenedifluoride) (PTFE) at a weight ratio of 95:5 on a titanium metal mesh (Alfa Aesar, 100 mesh). The areal loading of cathode material was ~38 mg cm^{-2}. The thickness of cathode is ~200 μm. Graphite anodes were fabricated by using mesocarbon

microbeads (MCMB) graphite powder (MTI Corp.) and poly(vinylidenedifluoride) (PTFE, Sigma-Aldrich) at a weight ratio of 9:1 on a stainless steel mesh (200 mesh).

Preparation of electrolytes. The liquid "water-in-bisalt" (WiBS) aqueous electrolytes were firstly prepared by dissolving 21 mol kg^{-1} lithium bis(trifluoromethanesulfonyl)imide (LiTFSI, >98%, TCI Co., Ltd.) and 7 mol kg^{-1} lithium trifluoromethanesulfonate (LiOTf (99.995%, Sigma-Aldrich) in water (HPLC grade). Aqueous gel electrolytes were prepared by mixing 20 wt.% poly(ethylene oxide) (PEO, average M_v ~ 600,000, Sigma-Aldrich) or 10 wt.% polyvinyl alcohol (PVA, M_w 146,000-186,000, 99+% hydrolyzed, Sigma-Aldrich) with WiBS electrolyte and heated at 80°C for 1 h in sealed glass molds. After cooling to the room temperature, sticky semi-solid WiBS gel electrolytes were obtained, which can be changed into any shape at 50 °C. The preparation of HFE-PEO gel protection coating was reported previously[2]. Briefly, the coating gel was prepared by mixing 1,1,2,2-tetrafluoroethyl-2',2',2'-trifluoroethyl ether (Daikin America or Apollo) with 0.5 M LiTFSI (denoted as LiTFSI-HFE gel) and 10 wt.% PEO in HFE/FEC (volume ratio = 95:5) and heated at 70°C for 5 min under strong stirring.

Preparation of chemical GICs as reference samples. The chemically intercalated Br_2 and BrCl GICs as reference samples were synthetized following the reported procedure[19,25]. Briefly, Br_2 and BrCl GICs were prepared by exposing the graphite flakes (TIMCAL TIMREX® KS4) in high-contraction Br_2 (99.99%, Sigma-Aldrich) vapor and BrCl gas in well-sealed flasks for 2 hours. BrCl was prepared by mixing the Br_2 with equimolar of Cl_2 at -70 °C, which obtained by the reaction of trichloroisocyanuric acid and hydrochloric acid. The as-prepared GICs were immediately transferred to Raman or XRD measurement to avoid the slow de-intercalations after being retracted from halogen gas atmosphere and exposed to atmosphere.

Electrochemical measurements. In the three-electrode cells, LBC-G electrodes (or other control electrodes) were used as working electrode, active carbon as counter electrode, and Ag/AgCl as reference electrode. The mass ratio of working electrode vs. electrolyte was 1:20. The three-electrode cells were then galvanostatically charged/discharged using a Land BT2000 battery test system (Wuhan, China) at room temperature. Cyclic voltammetry was carried out using a CHI 600E electrochemical work station. The GITT experiment was performed in a three-electrode device with the same electrode configuration. The cycling protocol consists of 80 mA g^{-1} (0.2 C) current pulses for 20 min alternated with 120 min OCV periods to reach quasi-

equilibrium potentials. The apparent ionic diffusion coefficients (D) of reactants in the LBC-G cathode at the different state of charge and discharge were estimated by the GITT measurement using the following relations[31]:

$$D = \frac{4}{\pi}\left(\frac{IV_m}{FS}\right)^2\left(\frac{dE/dx}{dE/dt^{1/2}}\right)^2 \quad (3)$$

where I is the applied constant current density, V_m is the molar volume of partially hydrated LiBr/LiCl, F is the Faraday constant (96,486 C mol^{-1}), S is the contact area between electrolyte and active materials, dE/dx is the slope of the coulometric titration curve at composition x and $dE/dt^{1/2}$ can be obtained from the plot of the transient voltage versus the square root of time during constant current pulse. The four-point EIS measurement was performed with Gamry 345 interface 1000 using 5 mV perturbation with the frequency range of 0.01 Hz to 100,000 Hz at room temperature. The ionic diffusion coefficient was calculated by simulation using equivalent circuit include finite Warburg element[32].

The full cells were assembled as CR2032-type coin cells using LBC-G as cathode and HFE-PEO gel protected graphite electrodes as anode. The cathode/anode mass ratios were set at 1.38:1. A titanium metal foil disk was applied between cathode and coin cell case to prevent corrosion. As-prepared WiBS gel electrolyte was press into films and applied in the coin cells as both electrolyte and separator. The mass ratio of total electrodes vs. electrolyte was in the range from 1:4 to 2:1. After assembly, the cell was briefly kept at 50 °C for GPE self-healing. The full cell was then cycled galvanostatically on a Land BT2000 battery test system (Wuhan, China) at room temperature.

The specific (gravimetric or volumetric) energy densities (E) of full cells were calculated by

$$E = C \times U \quad (4)$$

where C was the specific (gravimetric or volumetric) cell capacity and U was the average output cell voltage. The gravimetric capacity C_m was calculated by

$$C_m = \frac{C_{cell}}{m_{cathode}+m_{anode}} \quad (5)$$

where C_{cell} was the absolute cell capacity. $m_{cathode}$ was the total mass of cathode, including LiBr, LiCl, graphite and PTFE binder. m_{anode} was the total mass of anode, including graphite, PTFE binder and the polymer passivation coating.

***In situ* Raman studies.** For *in situ* Raman study, LBC-G/G full cell (in a coin cell configuration) was charged and discharged at 40 mA g^{-1} (0.1 C). A quartz optical window (ϕ = 5 mm) was applied on cathode side. Raman spectra were collected with a Horiba Jobin Yvon Labram Aramis using a laser (wavelength = 532 nm) between 3500 and 60 cm^{-1}. 4 × 4 points of data were collected to get high signal to noise ratios.

***Ex situ* and *in situ* XRD studies.** For *ex situ* X-ray diffraction (XRD) study, the LBC-G electrodes (working electrodes) were retracted from three-electrode cell after being charged/discharged to certain SOCs at 40 mA g^{-1} (0.1 C). For *in situ* X-ray diffraction (XRD) study, a full cell (in a coin cell configuration) was charged and discharged at 0.1 C. Kapton windows (ϕ = 3 mm) were applied on both sides of coin cells, where anode was deliberately placed to avoid the beam passage through the window. *Ex situ* X-ray diffraction patterns (Figure 3b) were recorded on Bruker D8 Advance X-ray diffraction, with Cu $K\alpha$ radiation in grazing-incidence geometry. High-energy synchrotron XRD measurements (Figure 3c-d) were carried out at the 11-ID-C beamline of the Advanced Photon Source (APS), Argonne National Laboratory. A high-energy X-ray with beam size of 0.2 mm × 0.2 mm and wavelength of 0.1173 Å was used to obtain two-dimensional (2D) diffraction patterns in the transmission geometry. X-ray patterns were recorded with a Perkin-Elmer large-area detector placed at 1800 mm from the battery cells. The interval between the consequent diffraction patterns was 5 min. The obtained 2D diffraction patterns were calibrated using a standard CeO_2 sample and converted to 1D patterns using Fit2D software.

The periodic repeat distance (I_C), the intercalant gallery height (d_i) of GICs can be calculated using[23]

$$I_C = d_i + 3.35\ \text{Å} \times (m - 1) = l \times d_{obs} \quad (6)$$

where l is the index of (0 0 l) planes oriented in the stacking direction and d_{obs} is the observed value of the spacing between two adjacent planes in XRD patterns, which can be calculated from diffraction angles by Bragg's law. The d spacing of pristine graphite is 3.35 Å. The intensity

pattern is commonly found for a stage *m* graphite intercalation compound (GIC), where the most dominant peak is the (0 0 *m*+1). The *d* spacing values of (0 0 *m*+1) were calculated from XRD data by Bragg's law (Extended Data Table 1), while the most dominant stage phase of the observed GIC can be assigned.

***Ex situ* XANES and EXAFS studies.** *Ex situ* X-ray absorption spectroscopy (XAS) measurements were conducted on the same cell configuration used for *in situ* XRD measurements. The experiments were carried out in transmission mode at the beamline 20-BM-B of APS, Argonne National Laboratory. The XANES measurements were performed at the K edge of bromine (13480 eV) and chlorine (2822 eV) to monitor the change of valence state of Br and Cl in cathode and the energy calibration was performed using the first derivative point of the XANES spectrum of Bi (L_{III}-edge = 13419 eV). During the Cl measurement, the entire X-ray beam, samples and detector were protected by helium gas. The reference spectra were collected for each spectrum by placing the bismuth metal foil in the reference channel. The EXAFS spectra were aligned, merged, and normalized using Athena[33,34]. The coin cells were charged to certain voltages with a constant current before the measurements.

Athena program was first used to process experimental X-ray absorption data to extract normalized oscillation amplitude $\chi^{exp}(k)$ and the photoelectron wave number k is defined by $k = \sqrt{2m(E - E_0)}/\square$, where E_0 is the absorption edge energy. The theoretical calculated χ^{th}(k) is given by EXAFS equation[35]:

$$\chi^{th}(k) = \sum_j \frac{S_0^2 N_j f_j(k)}{kR_j^2} e^{-2k^2\sigma_j^2} e^{-2r_j/\lambda(k)} sin[\,2kR_j + \delta_j(k, r_j)] \quad (7)$$

where j indicates the j^{th} shell with identical backscatters, N_j is the coordination number of the j^{th} shell, f_j is the backscattering amplitude, R_j is the average distance between the center atom and backscatters, σ_j is the mean square variation in R_j, δ_j is the scattering phase shift, λ is the effective mean free path and S_0^2 is the amplitude reduction factor, FEFF6 was used to calculate f_j, δ_j and λ. Fitting to the experimental data to refine structure parameters S_0^2, N_j, R_j, σ^2 is done using Artemis program. The initial crystal structures for fitting are starting from DFT optimized Stage II C_7[Br] and Stage I $C_{3.5}[Br_{0.5}Cl_{0.5}]$. S_0^2 was fixed at 1.0. Two ΔE were used in the fitting, one for the Br-Br (or Cl) paths, and the other one for the left Br-C paths.

Phase separation and water equilibrium studies. For water uptake estimation, WiBS liquid electrolyte was step-wisely (0.1 g each time) added into 20 mg of anhydrous LiBr/LiCl or LiBr/LiCl monohydrate mixed salts (20 mg, molar ratio = 1:1), along with 2 hours shake mixing and 6 hours standing (each time), until no solid residual was observed. For the demonstration of phase-separation, the as-prepared mixture aqueous solution of $LiBr{\cdot}3H_2O$ (0.8 g) and $LiCl{\cdot}3H_2O$ (0.4 g) was added into WiBS liquid electrolyte (3 g), following by 2 hours shake mixing and 1 hours standing. After 500 hours further exposure to LiCl/LiBr solution, small sample of WiBS was retracted and tested by anion exchange liquid chromatography (Dionex ICS-1100 Ion Chromatography System) for Br^- and Cl^- concentration.

SEM imaging and specific surface area measurement. SEM of the cycled cathode was performed in a Hitachi SU-70 with energy dispersive x-ray spectroscopy (EDS) operating at 5 kV. Specific surface areas of the samples were characterized by N_2 adsorption by means of a Micromeritics ASAP 2020 Porosimeter Test Station. Samples were degassed (in a vacuum) at 180 °C for 12 h before the test. The specific surface areas were calculated using the Brunauer–Emmett–Teller (BET) method from the adsorption branch.

Molecular dynamics simulations of LiBr in WiSE. MD simulations were performed on 18 m (mol salt/kg solvent) LiBr in water and a mixed salt 18m LiBr + 21m LiTFSI in water at 363 K. MD simulations utilized a previously modified CHARMM H_2O force field[47] in conjunction with the APPLE&P many-body polarizable force field for LiTFSI in H_2O that predicted ionic conductivity, ion and water self-diffusion coefficients, viscosity and density of LiTFSI-H_2O in excellent agreement with experiments over a wide range of salt concentrations from 5m to 21m[36]. APPLE&P functional form and combining rules are given elsewhere[37].

A parallel version of the in-house developed MD simulation package is used for MD simulations. The 18m LiBr in H_2O simulation cell contained 448 LiBr and 1390 H_2O molecules. The mixed salt MD simulation cell contained 1380 H_2O, 512 LiTFSI and 448 LiBr. All simulated $(LiTFSI)_g(LiBr)_h(H_2O)_i$ complexes resulting in large simulation cells of 70 and 95 Å. The simulation box dimensions were gradually decreased to 60 Å. NPT simulations were performed for 2 ns at 363 K for the mixed salt system at 363 K using a modified force field with the increased repulsion between Br/Br and TFSI/TFSI anions in order to evenly disperse them through the simulations box as shown in Extended Data Fig. 1e (left). After 9 ns of MD

simulations in NPT ensemble $LiBr(H_2O)_j$ largely separated from the $LiTFSI(H_2O)_k$ domain (right). Such behavior is indicative of the initial stages of phase-separation and is in accord with experimental observations.

The Ewald summation method was utilized in MD simulations for handling the electrostatic interactions between permanent charges with permanent charges and permanent charges with induced dipole moments with $k = 6^3$ vectors. Multiple timestep integration was employed with an inner timestep of 0.5 fs (bonded interactions); a central time step of 1.5 fs for all nonbonded interactions within a truncation distance of 7.0-8.0 Å and an outer timestep of 3.0 fs for all nonbonded interactions between 7.0 Å and the nonbonded truncation distance of the smaller of 19 Å. The reciprocal part of Ewald was updated only at the largest of the multiple time steps. A Nose-Hoover thermostat and a barostat were used to control the temperature and pressure with the associated frequencies of 10^{-2} and 0.1 x 10^{-4} fs. The atomic coordinates were saved every 2 ps for post-analysis.

Ability of MD simulations using atomic dipole polarizable APPLE&P force field to predict density and conductivity of 18m LiBr in H_2O was examined at 333 K. After 3 ns equilibration in NPT ensemble, 8 ns MD simulations in NVT ensemble predicted electrolyte density of 1649 kg m^{-3}, which is 0.8% higher than experimental density of 1636.5 kg m^{-3}.[38] Ionic conductivity (σ) was extracted using the Einstein relations shown in eq. 8:

$$\sigma = \lim_{t\to\infty} \frac{e^2}{6tVk_BT} \int_{i,j}^{N} z_i z_j < ([\boldsymbol{R}_i(t) - \boldsymbol{R}_i(0)])([\boldsymbol{R}_j(t) - \boldsymbol{R}_j(0)]) > \quad (8)$$

where e is the electron charge, V is the volume of the simulation box, k_B is Boltzmann's constant, T is the temperature, t is time, z_i and z_j are the Li^+ and Br^- charges, $R_i(t)$ is the displacement of the ion i during time t, < > denote the ensemble average and N is the number of diffusing. Due to the finite size of the simulation cell, long range hydrodynamic interactions restrict diffusion. The leading order finite size correction (FSC)[37,39] to the self-diffusion coefficient is given by eq.9

$$\Delta D^{FSC} = \frac{2.837 k_B T}{6\pi\eta L} \quad (9)$$

where k_B is the Boltzmann constant, T is temperature, L is a linear dimension of the simulation periodic cell and is viscosity. After FCS correction, MD simulations predicted conductivity of 18m LiBr electrolyte to be 75 mS/cm that is 30% lower than the experimentally determined conductivity of 98.89 mS/cm but is sufficiently accurate for the highly concentrated electrolyte.

DFT simulations of intercalation structure configuration. All calculations were performed using DFT with a plane wave basis set and the projector augmented wave (PAW)[40] method, as implemented in the Vienna *Ab* Initio Simulation Package (VASP)[41]. The Perdew-Burke-Ernzerhof (PBE) functional in the Generalized Gradient Approximation (GGA)[42] is employed to calculate the exchange-correlation energy. An energy cutoff of 580 eV was used for the plane wave basis, and the Brillouin zone was sampled using the Monkhorst-Pack scheme. The van der Waals density functional (vdW-DF) of optB86b[43] is used to correct Van der Waals energies to get accurate interlayer spacing values in all cases. According to the previous work, two sets of possible configurations for C_7[Br], $C_{3.5}$[$Br_{0.5}Cl_{0.5}$] and C_8[Br], C_4[$Br_{0.5}Cl_{0.5}$] were taken into consideration[26,44]. In these configurations the Br and Cl atoms were initialized randomly. The geometry optimizations were performed using the conjugated gradient method, and the convergence threshold is set to be 10^{-5} eV in energy and 0.01 eV/Å in force. The charge difference plots were obtained by subtracting the charge density of both graphite and Br (BrCl) from the charge density of C_7[Br] ($C_{3.5}$[$Br_{0.5}Cl_{0.5}$]), respectively. The charge distribution on the atoms were determined using the Bader analysis method[45]. Visualization of the structures were made using VESTA software[46].

Intercalation voltage step profile simulation. Intercalation voltage profiles were computed with CP2K v5.1[47] using the dispersion corrected (D3)[48,49] PBE[50] functional and double-ζ (triple-ζ for bromide) short-range, molecularly optimized valence basis sets[51] and appropriate Goedecker-Teter-Hutter (GTH) pseudopotentials[52,53] for core electrons. The plane wave energy cutoff was set to 1000 Ry and the Brillouin zone was sampled at the Γ point only. Geometry and cell optimizations were converged to a max change in atomic positions between steps of 0.0005 au. The other convergence criteria were left at their defaults.

The intercalation voltage (E_{int}) against Li^+/Li is computed from a series of energy calculations, assuming a negligible entropic contribution, as

$$E_{int} = \frac{E(GrX) - E(Gr) + n_X E_{desolv}(LiX) - n_X E_{gas}(LiX) + n_X E_b(Li)}{n_X} \quad (10)$$

Above, n_x is the number of anions, E(GrX) the energy of the intercalated graphite gallery, E(Gr) the energy of pure graphite in AB-stacking, E_{desolv}(LiX) the desolvation energy of a LiX contact ion pair using the cluster-continuum method (with up to 8 explicit waters) from Gaussian[54]

calculations with PBEPBE+D3/6-31G(d),[42,48,49,55] E_{gas}(LiX) the energy of the LiX contact ion pair in a 10 Å × 10 Å × 10 Å cell, and E_b(Li) the energy per Li in bulk metal (-204.1894 eV/Li). For stages I-IV and VI, 12 layers of carbon were modeled. Stage V was modeled with 10 layers of carbon. Each layer consisted of 112 carbon atoms.

Methods Reference:

31 Wen, C. J., Boukamp, B. A., Huggins, R. A. & Weppner, W. Thermodynamic and Mass Transport Properties of "LiAl". *Journal of The Electrochemical Society* **126**, 2258-2266 (1979).

32 Barsoukov, E. & Macdonald, J. R. *Impedance spectroscopy: theory, experiment, and applications*. (John Wiley & Sons, 2018).

33 Ravel, B. & Newville, M. ATHENA, ARTEMIS, HEPHAESTUS: data analysis for X-ray absorption spectroscopy using IFEFFIT. *Journal of Synchrotron Radiation* **12**, 537-541 (2005).

34 Newville, M. EXAFS analysis using FEFF and FEFFIT. *Journal of Synchrotron Radiation* **8**, 96-100 (2001).

35 Bunker, G. *Introduction to XAFS: a practical guide to X-ray absorption fine structure spectroscopy*. (Cambridge University Press, 2010).

36 Borodin, O. *et al.* Liquid Structure with Nano-Heterogeneity Promotes Cationic Transport in Concentrated Electrolytes. *ACS Nano* **11**, 10462-10471 (2017).

37 Borodin, O. Polarizable force field development and molecular dynamics simulations of ionic liquids. *The Journal of Physical Chemistry B* **113**, 11463-11478 (2009).

38 Zaytsev, I. D. & Aseyev, G. G. *Properties of aqueous solutions of electrolytes*. (CRC press, 1992).

39 Dünweg, B. & Kremer, K. Molecular dynamics simulation of a polymer chain in solution. *The Journal of chemical physics* **99**, 6983-6997 (1993).

40 Blöchl, P. E. Projector augmented-wave method. *Physical review B* **50**, 17953 (1994).

41 Kresse, G. & Hafner, J. Ab initio molecular-dynamics simulation of the liquid-metal–amorphous-semiconductor transition in germanium. *Physical Review B* **49**, 14251 (1994).

42 Perdew, J. P., Burke, K. & Ernzerhof, M. Generalized gradient approximation made simple. *Physical review letters* **77**, 3865 (1996).

43 Klimeš, J., Bowler, D. R. & Michaelides, A. Chemical accuracy for the van der Waals density functional. *Journal of Physics: Condensed Matter* **22**, 022201 (2009).

44 Ghosh, D. & Chung, D. D. L. Two-dimensional structure of bromine intercalated graphite. *Materials Research Bulletin* **18**, 1179-1187 (1983).

45 Henkelman, G., Arnaldsson, A. & Jónsson, H. A fast and robust algorithm for Bader decomposition of charge density. *Computational Materials Science* **36**, 354-360 (2006).

46 Momma, K. & Izumi, F. VESTA 3 for three-dimensional visualization of crystal, volumetric and morphology data. *Journal of applied crystallography* **44**, 1272-1276 (2011).

47 Hutter, J., Iannuzzi, M., Schiffmann, F. & VandeVondele, J. CP2K: atomistic simulations of condensed matter systems. *Wiley Interdisciplinary Reviews: Computational Molecular Science* **4**, 15-25 (2014).

48 Grimme, S., Antony, J., Ehrlich, S. & Krieg, H. A consistent and accurate ab initio parametrization of density functional dispersion correction (DFT-D) for the 94 elements H-Pu. *The Journal of chemical physics* **132**, 154104 (2010).
49 Grimme, S., Ehrlich, S. & Goerigk, L. Effect of the damping function in dispersion corrected density functional theory. *Journal of computational chemistry* **32**, 1456-1465 (2011).
50 Zhang, Y. & Yang, W. Comment on "Generalized gradient approximation made simple". *Physical Review Letters* **80**, 890 (1998).
51 VandeVondele, J. & Hutter, J. Gaussian basis sets for accurate calculations on molecular systems in gas and condensed phases. *The Journal of chemical physics* **127**, 114105 (2007).
52 Goedecker, S., Teter, M. & Hutter, J. Separable dual-space Gaussian pseudopotentials. *Physical Review B* **54**, 1703 (1996).
53 Hartwigsen, C., Gœdecker, S. & Hutter, J. Relativistic separable dual-space Gaussian pseudopotentials from H to Rn. *Physical Review B* **58**, 3641 (1998).
54 Frisch, M. J. *et al.* Gaussian 09, revision A. 1. *Gaussian Inc. Wallingford CT* **27**, 34 (2009).
55 Francl, M. M. *et al.* Self‐consistent molecular orbital methods. XXIII. A polarization‐type basis set for second‐row elements. *The Journal of Chemical Physics* **77**, 3654-3665 (1982).

Data availability

The data that support the findings of this study are available from the corresponding authors on request.

Figure legends

Figure 1 | New conversion-intercalation chemistry. a, Schematic drawing of the conversion-intercalation mechanism occurring in LBC-G composite during its oxidation in WiBS aqueous-gel electrolyte. The two-stage reactions involved the oxidation of Br^- (~4.0 V) and Cl^- (~4.2 V) and their subsequent intercalation into graphitic structure. The discharge was a complete reversal of the charge process. **b**, Cyclic voltammogram of LBC-G cathode between 3.2 and 4.9 V vs. Li/Li^+ at scan rate of 0.05 mVs^{-1}. **c**, Galvanostatic charge/discharge profiles of LBC-G cathode at a current density of 80 mA g^{-1}. Insert: Discharge capacity retention and coulombic efficiencies. **d**, The comparison between the predicted intercalation voltage from density functional theory (DFT) simulations and the quasi-equilibrium voltage curves obtained from GITT measurement (Figure 1e). The data points of simulations are stage VI $C_{20}[Br]$, stage V $C_{17.5}[Br]$, stage IV $C_{14}[Br]$, stage III $C_{10.5}[Br]$, and stage II $C_7[Br]$ (A), stage I $C_{3.5}[Br_{0.9375}Cl_{0.0625}]$ (B), stage I $C_{3.5}[Br_{0.875}Cl_{0.125}]$ (C), stage I $C_{3.5}[Br_{0.75}Cl_{0.25}]$ (D), stage I $C_{3.5}[Br_{0.625}Cl_{0.375}]$ (E), stage I $C_{3.5}[Br_{0.5}Cl_{0.5}]$ (F). **e**, GITT characterization of LBC-G cathode at a current density of 80 mA g^{-1}. Red curve is quasi-equilibrium potential at different lithiation/de-lithiation stages, which was constructed from the average value of each open-circuit voltage period during charge/discharge. Inset: The finite diffusion coefficients *D* of reactants estimated from GITT and EIS measurements (see Methods). **f**, Nyquist plots for LBC-G cathode obtained by EIS

tests at various SOCs in a three-electrode cell. The dashed lines are the fitting curve by using the equivalent circuit which is shown in Extended Data Figure 4a. Inset: plots in a full scale. **g**, Practical gravimetric energy density of LBC-G cathode compared with a few representative state-of-the-art cathodes with average discharge voltages referred to Li/Li^+. Intercalation-type[6]: $LiFePO_4$ (LFP), $LiCoO_2$ (LCO), $LiNi_{0.8}Co_{0.15}Al_{0.05}O_2$ (NCA), $LiNi_{0.8}Co_{0.1}Mn_{0.1}O_2$ (NCM); conversion-type[9,12]: FeF_2, $Cu_{0.5}Fe_{0.5}F$, Li_2S. The values were calculated from the reversible gravimetric capacities based on the total mass of cathode (including active, inactive and polymeric binder) and average discharge voltages. The mass ratios of active materials: 80% for intercalation-type, 70% for metal fluorides, and 50% for sulfur.

Figure 2 | Br and Cl conversion-intercalation mechanism. a, *In situ* Raman spectra (100 – 550 cm^{-1}) of LBC-G during the entire charge–discharge cycle, showing the evolutions of Br_2 and BrCl intercalants. Red line: Free BrCl signals detected only after deliberately destabilizing the graphite host with a strong laser beam, further confirming the BrCl intercalation. Background from quartz was removed. **b**, *Ex situ* Br K-edge XANES of LBC-G composite during its first charging process. Chemically intercalated Br_2 and liquid Br_2 as control samples (dash curves) were measured in the same cell configuration. **c**, *Ex situ* Cl K-edge XANES of LBC-G composite during its first charging process. **d**, Iso-surface of the charge density difference for GICs C_n[Br] (top) and C_n[BrCl] (bottom) obtained from DFT simulations. Yellow and blue regions represent the accumulation and depletion of electrons when compared to Br_2 and BrCl gas molecules (iso-value of ± 0.0006 *e* $Å^{-3}$), respectively. The oxidation states obtained from Bader analysis are: -0.16 for Br in C_n[Br]; -0.05 for Br and -0.25 for Cl in C_n[BrCl]. **c**, Schematic drawing of the corresponding GICs with different stage number *m*. **e**, **f**, The charge/discharge profiles of LBC-G composites with various mole ratios of LiBr/LiCl after the first charge at the current density of 80 mA g^{-1}. The specific capacities were estimated by the weight of LiBr and LiCl. The mole ratios were changed by only reducing the certain portions of LiCl(**e**) or LiBr(**f**) from the original LiBr/LiCl/graphite composites.

Figure 3 | The staging structure and in-plane configurations of halogen GICs. a, *In situ* Raman spectra (1200 – 2850 cm^{-1}) of LBC-G during the entire charge–discharge cycle, showing the graphite structure evolution with Br_2 and BrCl intercalation/de-intercalation. **b**, *Ex situ* XRD of LBC-G composite in various charging and discharging states through the second cycle. θ-2θ scan mode was employed with Cu Kα radiation (1.5418 Å) in reflection geometry. Left: overall spectra. Middle: magnified range of 2θ (24°–28°). Right: magnified range of 2θ (48°–60°). The peaks of titanium current collectors were used to calibrate the displacement error. **c**, *In situ* XRD patterns of (*0 0 m+1*) peak for LBC-G composite during a charge–discharge cycle, which were collected with high-energy X-ray radiation (wavelength of 0.1173 Å) in transmission geometry. Left: Corresponding voltage profile. Right: 2D contour of XRD patterns and representative curves illustrating the continuous evolution of *d* spacing (3.30–3.55 Å) for graphite host during intercalation/de-intercalation. The 2θ diffraction angles were converted to *d* spacing for convenience (see Methods). **d**, *Ex situ* High-energy XRD patterns for LBC-G composites (electrolyte and current collector removed) at 50% and 100% SOCs. High-energy transmission X-ray radiation (0.1173 Å) was set perpendicular to most of graphite flakes to reveal in-plane structure features. **e-f,** The best-fit modes for Br EXAFS experimental data of Stage II C_7[Br] (**e**, SOC = 50%) and Stage I $C_{3.5}[Br_{0.5}Cl_{0.5}]$ (**f**, SOC = 100%), respectively. The

EXAFS spectra here in *R* Space are phase-uncorrected, so that the distance *R* in two Figures for two stages are not comparable but both are smaller than the actual values. Inset: In-plane configurations of Stage II $C_7[Br]$ and Stage I $C_{3.5}[Br_{0.5}Cl_{0.5}]$ obtained from DFT simulations. Two sets of bond distances were marked as red lines (short) and blue lines (long).

Figure 4 | High-energy-density aqueous LIBs with LBC-G cathodes. a, Typical charge-discharge voltage profiles (the 3rd cycles) of two Li-ion full cells with LBC-G cathodes consisting of anhydrous LiBr/LiCl (blue) or LiBr/LiCl monohydrates (red) and HFE/PEO protected graphite anodes. Charging and discharging were performed at 0.2 C (44 mA g^{-1} for LBC-G cathode) at 25 °C. The cell capacity was calculated based on the cathode mass alone (upper X-axis) or the total mass of cathode and anode including binder and protective coating (bottom x-axis). **b**, The discharge capacities (on total mass of cathode and anode, open circles) and coulombic efficiencies (semi-solid circles) of these full cells during cycling. **c**, Discharge capacities calculated on total anode and cathode mass at various rates of these LBC-G/graphite full cells with different electrolyte/electrodes (cathode + anode) mass ratios. **d**, Actual (red star) energy densities of LBC-G full cells (with LiBr/LiCl monohydrates) as compared with various state-of-the-art commercial and experimental Li-ion chemistries using both non-aqueous (blue circles) and aqueous (green circles) electrolytes. For comparison, all energy densities were converted based on the total weight of the positive and negative electrodes (not counting electrolyte and cell-packaging).

Extended Data Legends

Extended Data Figure 1| Immiscibility of LiBr and LiCl in WiBS aqueous electrolyte. a, Visual observations of the hydration of anhydrous LiBr/LiCl mixed salts (20 mg, molar ratio = 1:1) in 2 g (left) and 5.1 g (right) of WiBS liquid electrolyte. **b**, Visual observations of the hydration of LiBr/LiCl monohydrate mixed salts (20 mg, molar ratio = 1:1) in 1.5 g (left) and 3.0 g (right) of WiBS liquid electrolyte. The solid residue was marked by dash cycle. **c**, Visual observation of the immiscibility (clear phase-separation) for the as-prepared mixture aqueous solution (top) of $LiBr{\cdot}3H_2O$ (0.8 g) and $LiCl{\cdot}3H_2O$ (0.4 g) in WiBS liquid electrolyte (bottom, 3 g). **d**, Only trace concentrations (< 35 p.p.m) of Br^- and Cl^- are detected in the WiBS liquid electrolyte by using anion exchange liquid chromatography after 500 hours exposure to LiBr/LiCl solution. **e,** MD simulation cell snapshots containing initial configuration (left) and final (right) after 9 ns run for the 18 mol kg^{-1} LiBr – 21 mol kg^{-1} LiTFSI in H_2O at 363 K with the Br^- anions highlighted.

Extended Data Figure 2| The solid states of LiBr and LiCl in LBC-G cathode. a-c, Scanning electron microscope (SEM) (**a**) and Br (**b**), Cl (**c**) energy-dispersive X-ray spectroscopy (EDS) mapping images of LBC-G composite cathode, showing the morphology and distributions of LiCl and LiBr in the cathode layer after 5 full cycles. Distributions of Br and Cl are overlapping, indicating that two salts are well mixed as result of their close association during the co-intercalation/de-intercalation. **d**, *Ex situ* X-ray diffraction patterns of LBC-G cathode retracted from cycled cells after the 5th charge and discharge. The disappearance of LiBr and LiCl peaks and appearance of GIC peaks of LBC-G cathode confirm the BrCl intercalation reaction at fully charged state, while the

typical patterns of crystalline LiBr and LiCl at fully discharged state suggested that solid LiBr and LiCl are reformed after de-intercalation of halogen anions from graphite. The (002) peak of graphite with extremely high intensity was cut off in order to show the rest of other peaks. **e**, The potential of LBC-G cathode during discharge, open-circuit relaxation in 40-hour rest and charge process at 0.2C. The complete recovery of charge capacity in next cycle showed that all the active LiBr and LiCl material well-confined in the LBC-G cathode and absolutely no capacity loss during the long- time rest. **f,** The OCV decays in 40-hour rest of the LBC-G cathode at fully charged state of 4.5 V at 0.2C, respectively. The self-discharge was evaluated by comparison with the coulombic efficiency and the capacity loss after resting.

Extended Data Figure 3| Absence of corrosion of the current collector and oxidations of graphite and water in the operation potentials. a Linear sweep voltammetry of pure graphite electrode (with only PTFE binder) on Ti mesh current collector in $LiBr{\cdot}3H_2O$, $LiCl{\cdot}3H_2O$, and WiBS electrolyte with Ag/AgCl electrode as reference at 1 mV/s, show absence of side reactions including corrosion of the current collector and oxidations of graphite and water before the onsets at ~ 4.0 V, 4.5 V and 5.0 V vs. Li/Li+, in according with the oxidations of Br-, Cl-, and water, respectively. (**b)** C *1s* XPS and (**c**) Overall (Binding energy: 0 eV ~ 293 eV) of the LBC-G cathode before and after 10 full cycles. LiBr and LiCl were removed to avoid interference. No carbon-oxygen or carbon-halogen bonds were observed. Only trace of Br was detected as intercalation residual based on the low amount.

Extended Data Figure 4| Nyquist plot fitting, volumetric energy density and full cell configuration. a, Equivalent circuit used in fitting Nyquist plots in Figure 1f, consisting of ohmic resistance R1, a constant phase element (CPE1) parallel with a resistor (R2) which is connected with a finite diffusion Warburg (Ws1) in series. Note: the open Warburg at the end of the plot was not include, the data at low frequency was truncated accordingly during fitting. **b**, The comparison of Nyquist plots of the LBC-G cathodes containing of graphite hosts with different average flake sizes (~4 μm and ~800 μm), showing the independence of diffusion kinetics on halogen diffusion length inside of graphite interlayer. **c**, Practical volumetric energy density of LBC-G cathode compared with those of other representative state-of-the-art cathodes when paired with Li metal anodes. For the fair comparisons, a unit stack (the smallest cell unit) comprised 100 μm thick cathode, 9 mm separator and Li metal anode calculated based on the capacity matching. The volume fraction of the active material in each electrode is considered to be 70 vol.% in the case of intercalation materials, and 60 vol.% in the case of conversion-type cathodes. Material properties in the fully expanded (lithiated) state were used for calculating the volumetric capacities and inactive volume within each electrode. Areal capacities of anodes and cathodes were matched 1 : 1 and no extra capacity was considered for the formation losses. **d-e**, Schematic drawing of the full cell configurations with LBC-G composite cathode in WiBS aqueous-gel electrolyte at (**d**) charging and (**e**) discharging.

Extended Data Figure 5| The reversible halide redox chemistry enabled by intercalation in graphite. Galvanostatic charge and discharge profiles of different composite cathodes at the current density of 80 mA g^{-1} in WiBS gel electrolyte: **a**, LiBr-graphite (mass ratio ~1:1) cathode at the potential range of 3.20 V – 4.62 V. Without the presence of Cl^-, there was no further oxidation reactions of Br^0 until the potential raised to higher than 4.55 V vs. Li/Li^+, in which Br^0 is further irreversibly oxidized into BrO^-. **b**, $(LiBr)_{0.5}(LiCl)_{0.5}$/titanium nanopowder (mass ratio

= 1:20) composite, showing a charge capacity as 85% of theoretical value for halogen anion redox reactions and negligible discharge capacity. The higher overpotential might be due to the lack of carbon catalysis for redox reactions. **c**, $(LiBr)_{0.5}(LiCl)_{0.5}$/graphitized carbon black (mass ratio = 1:3). **d,** $(LiBr)_{0.5}(LiCl)_{0.5}$/active carbon (mass ratio = 1:3). **e**, $(LiBr)_{0.5}(LiCl)_{0.5}$/KS4 (mass ratio = 6:4). N_2 absorption/desorption isotherm of (**f**) graphite (KS4) electrode and (**g**) active carbon electrode with 5 wt.% PTFE binder. It indicated that graphite host cannot provide large surface area and small size pores as active carbon to store halogens by adsorption. **h**, *Ex situ* XRD of LiBr/LiCl/active carbon cathodes at fully charged and discharged states. After the adsorbing halogen (Br_2 and BrCl) during the charging, a relatively strong peak appeared at the (002) peak area, and (100) was weaken. It might imply the reformation of randomly oriented small graphitic zones with the help of halogen integration, which indicated minor contribution for halogens storage from intercalation-like behavior into nano-graphitize grain.

Extended Data Figure 6| The reference samples of chemically intercalated halogen GICs. X-ray diffraction patterns (XRD) of home-made chemically intercalated (**a-c**) Br_2 and (**d-f**) BrCl GICs as reference samples. These GICs were prepared by exposing the graphite flakes in high-contraction Br_2 vapor and BrCl gas for 2 hours. See more synthesis details in Methods. The spontaneous slow de-intercalations of XRD peaks in 48 h were observed by θ-2θ scan mode with Cu$K\alpha$ radiation (1.5418 Å) in reflection geometry. **g**, Raman spectra (50 cm^{-1} – 500 cm^{-1}) of chemically intercalated Br_2 and BrCl GICs as reference samples.

Extended Data Figure 7| The representative structures of stage I $[Br_{0.5}Cl_{0.5}]C_{3.5}$ complex obtained from DFT simulations. All structures have intercalation voltages within 0.02 V per ion of a structure assuming homogenous Br-Cl-Br-Cl bond lengths at 2.45 □ (top left). The bottom right structure is simulated based on the reported Br_2 structure[28]. Quantum chemistry calculations performed on the Cl-Br..Cl-Br cluster surrounded by conductive polarized continuum also yielded the zig-zig configuration for the Cl-Br…Cl-Br complex with the Cl-Br…Cl-Br angle around 110º having a lower energy than the linear Cl-Br...Cl-Br configuration by 0.1 eV from MP2/aug-cc-pvTz and PBE/aug-cc-pvTz calculations. The most stable geometry from these cluster calculations is similar to the one found in the stage I complexes shown above.

Extended Data Figure 8| The stage I $[Br_{0.5}Cl_{0.5}]C_{3.5}$ complex structures obtained from *ab initio* MD simulations. Results from 30 ps of constant volume (NVT ensemble) *ab initio* MD simulations using CP2K package starting from a structure with homogenous -Br-Cl- bond lengths as it was the most computationally efficient to work with. **a, (left)** radial distribution function (RDF) g(r) of stage I $[Br_{0.5}Cl_{0.5}]C_{3.5}$ from 30 ps of dynamics at 333 K **(right)** final snapshot of the trajectory. **b, (left)** DFT of stage I $[Br_{0.5}Cl_{0.5}]C_{3.5}$ from 30 ps of dynamics at 333 K, following an initial annealing to 633 K to accelerate appearance of disorder **(right)** final snapshot of the trajectory, close Br-Br contact highlighted in red oval. No close Cl-Cl contacts form at this voltage, as evidenced by the absence of features near the gas phase Cl-Cl bond length in the RDF. NVT simulations utilized Langevin thermostat with the associated time constant of 10 fs and average box dimensions obtained from the equilibration runs performed in constant pressure and temperature ensemble (NPT) for 100 ps. A 1 fs timestep was used throughout. No signs of gassing and subsequent graphite exfoliation were observed over 100 ps of additional simulation under constant pressure conditions, even after a brief annealing to 633 K and relaxation back to 333 K.

Extended Data Figure 9| The representative in-plane configurations of the cathode structure from DFT calculations. Stage II C_7[Br] cathode (**a**), Stage I C_7[BrCl] (**b**), Stage II C_8[Br] (**c**) and Stage I C_8[BrCl] (**d**) obtained from DFT simulations. Only a set of bond lengths can be obtained by this C_4[X] stoichiometry (X = halogen). Comparison of the scattering paths calculated using FEFF6 based on different DFT structures: stage II ((**e**) C_7[Br] vs. (**f**) C_8[Br]) and stage I ((**g**) $C_{3.5}[Br_{0.5}Cl_{0.5}]$ vs. (**h**) $C_4[Br_{0.5}Cl_{0.5}]$) to determine the best modes for fitting the experimental XAFS data. The nearest (black curve), the second nearest (red curve), and the third nearest (blue curve) scattering paths around the Br center were shown here. The absence of the second nearest Br-Br (R ~ 2.6 Å) or Br-Cl (R ~ 2.6 Å) scattering paths for C_4[X] stoichiometry suggested that it would be the dominant one in the real materials.

Extended Data Table 1| Calculated values of d spacing, stage numbers and plane index of Br_2 and BrCl GICs. The values corresponding to the dominant XRD peaks were marked as red. The values were calculated by eq. 6.

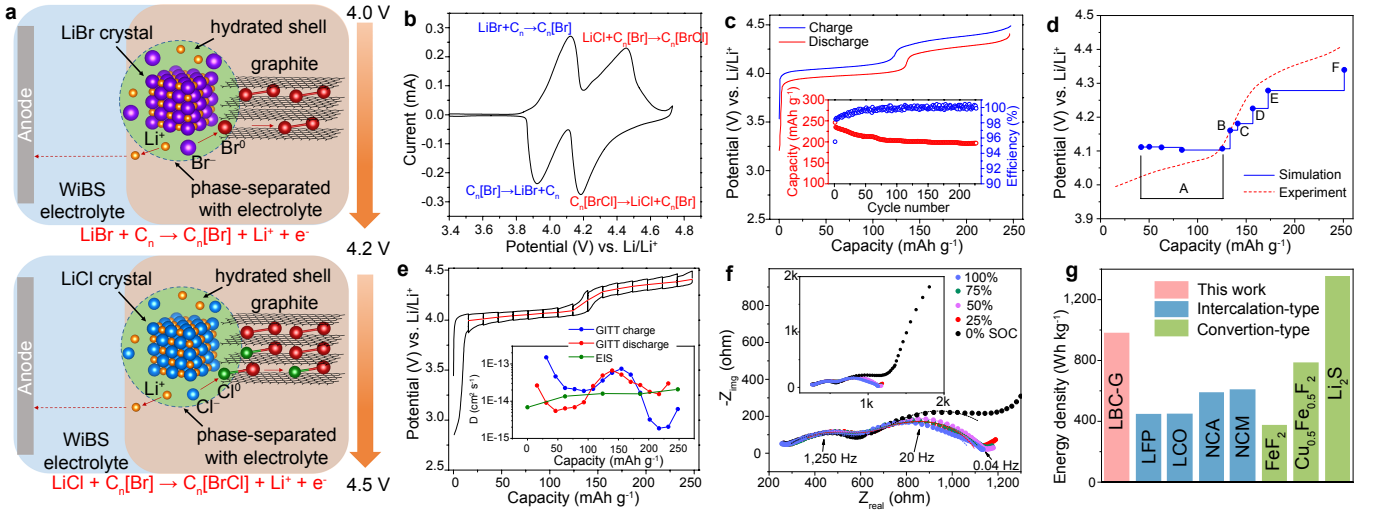
a
LiBr crystal
hydrated shell
graphite
Anode
Li+
Br–
Br0
WiBS electrolyte
phase-separated with electrolyte
4.0 V
LiBr + Cn → Cn[Br] + Li+ + e-
4.2 V
LiCl crystal
hydrated shell
graphite
Anode
Li+
Cl–
Cl0
WiBS electrolyte
phase-separated with electrolyte
LiCl + Cn[Br] → Cn[BrCl] + Li+ + e-
4.5 V
b
LiBr+Cn→Cn[Br]
LiCl+Cn[Br]→Cn[BrCl]
Cn[Br]→LiBr+Cn
Cn[BrCl]→LiCl+Cn[Br]
Current (mA)
Potential (V) vs. Li/Li+
c
Charge
Discharge
Potential (V) vs. Li/Li+
Capacity (mAh g-1)
Capacity (mAh g-1)
Efficiency (%)
Cycle number
d
Potential (V) vs. Li/Li+
Capacity (mAh g-1)
A
B
C
D
E
F
Simulation
Experiment
e
Potential (V) vs. Li/Li+
Capacity (mAh g-1)
GITT charge
GITT discharge
EIS
D (cm2 s-1)
f
100%
75%
50%
25%
0% SOC
-Zimg (ohm)
Zreal (ohm)
1,250 Hz
20 Hz
0.04 Hz
g
This work
Intercalation-type
Convertion-type
Energy density (Wh kg-1)
LBC-G
LFP
LCO
NCA
NCM
FeF2
Cu0.5Fe0.5F2
Li2S

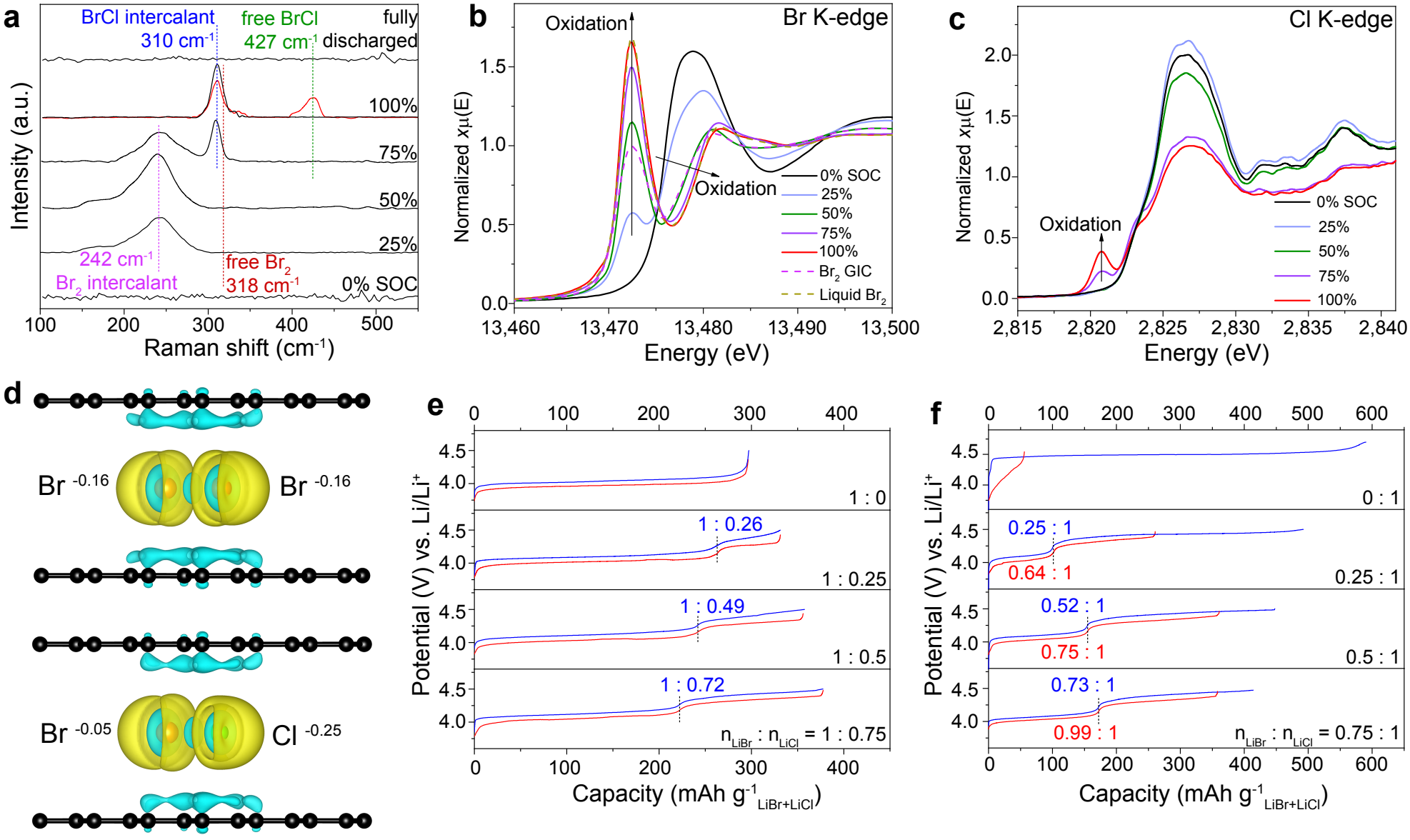
a
BrCl intercalant
310 cm-1
free BrCl
427 cm-1
fully discharged
100%
75%
50%
25%
242 cm-1
Br2 intercalant
free Br2
318 cm-1
0% SOC
Intensity (a.u.)
Raman shift (cm-1)
b
Br K-edge
Oxidation
Oxidation
Normalized xμ(E)
Energy (eV)
0% SOC
25%
50%
75%
100%
Br2 GIC
Liquid Br2
c
Cl K-edge
Oxidation
Normalized xμ(E)
Energy (eV)
0% SOC
25%
50%
75%
100%
d
Br -0.16
Br -0.16
Br -0.05
Cl -0.25
e
Potential (V) vs. Li/Li+
Capacity (mAh g-1 LiBr+LiCl)
1 : 0
1 : 0.26
1 : 0.25
1 : 0.49
1 : 0.5
1 : 0.72
nLiBr : nLiCl = 1 : 0.75
f
Potential (V) vs. Li/Li+
Capacity (mAh g-1 LiBr+LiCl)
0 : 1
0.25 : 1
0.64 : 1
0.25 : 1
0.52 : 1
0.75 : 1
0.5 : 1
0.73 : 1
0.99 : 1
nLiBr : nLiCl = 0.75 : 1

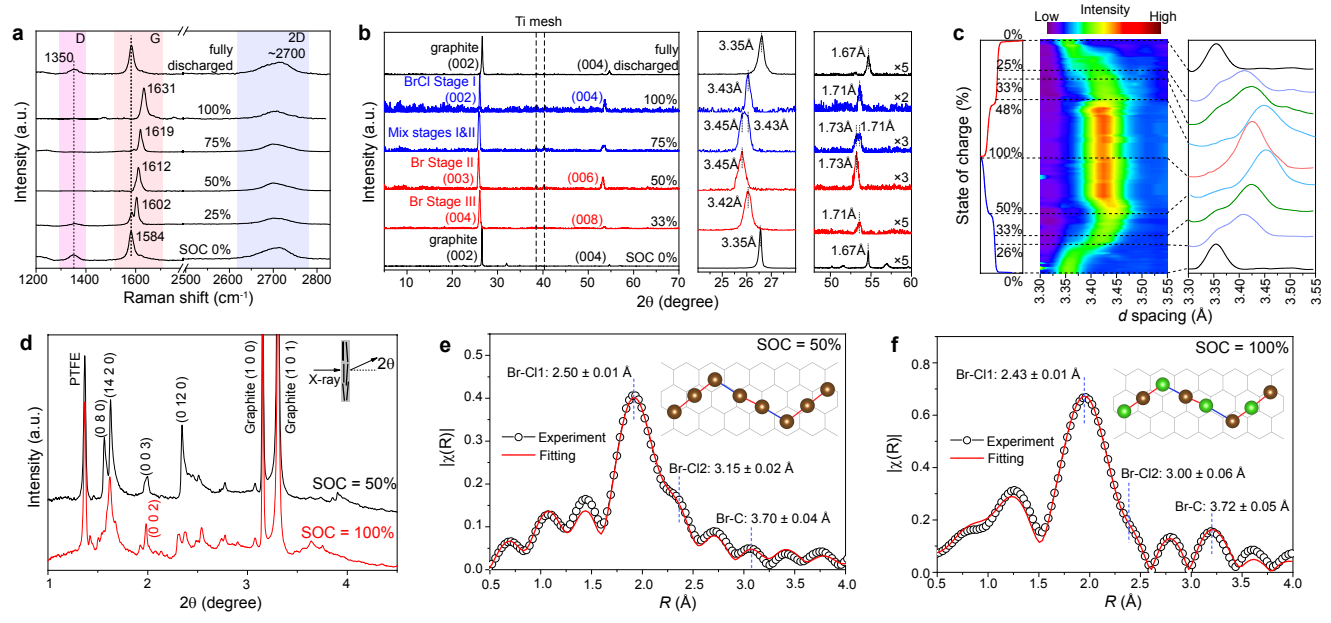
a
D
G
2D
1350
fully discharged
~2700
1631
100%
1619
75%
1612
50%
1602
25%
1584
SOC 0%
Intensity (a.u.)
Raman shift (cm⁻¹)
b
Ti mesh
graphite (002)
fully (004) discharged
BrCl Stage I (002)
(004)
100%
Mix stages I&II
75%
Br Stage II (003)
(006)
50%
Br Stage III (004)
(008)
33%
graphite (002)
(004)
SOC 0%
3.35Å
3.43Å
3.45Å
3.43Å
3.45Å
3.42Å
3.35Å
1.67Å
×5
1.71Å
×2
1.73Å
1.71Å
×3
1.73Å
×3
1.71Å
×5
1.67Å
×5
Intensity (a.u.)
2θ (degree)
c
Low
Intensity
High
0%
25%
33%
48%
100%
50%
33%
26%
0%
State of charge (%)
d spacing (Å)
d
PTFE
(0 8 0)
(14 2 0)
(0 0 3)
(0 0 2)
(0 12 0)
Graphite (1 0 0)
Graphite (1 0 1)
X-ray
2θ
SOC = 50%
SOC = 100%
Intensity (a.u.)
2θ (degree)
e
SOC = 50%
Br-Cl1: 2.50 ± 0.01 Å
Experiment
Fitting
Br-Cl2: 3.15 ± 0.02 Å
Br-C: 3.70 ± 0.04 Å
|χ(R)|
R (Å)
f
SOC = 100%
Br-Cl1: 2.43 ± 0.01 Å
Experiment
Fitting
Br-Cl2: 3.00 ± 0.06 Å
Br-C: 3.72 ± 0.05 Å
|χ(R)|
R (Å)

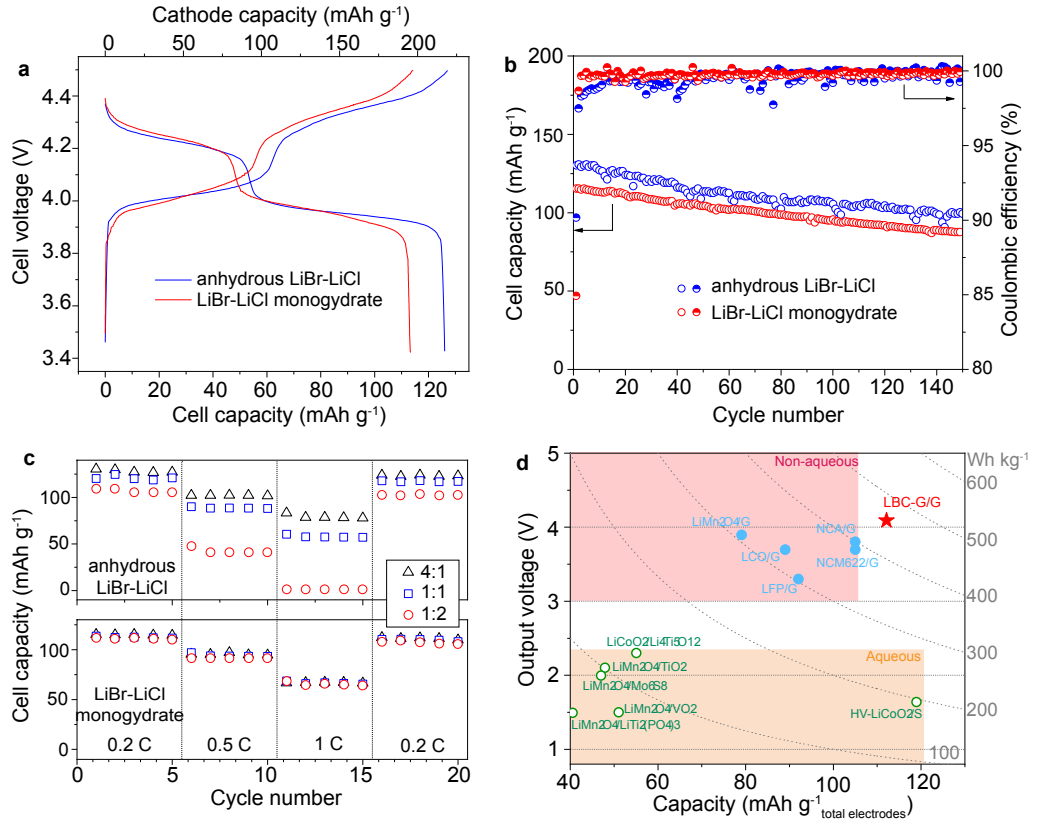
a
Cathode capacity (mAh g-1)
Cell voltage (V)
Cell capacity (mAh g-1)
anhydrous LiBr-LiCl
LiBr-LiCl monogydrate
b
Cell capacity (mAh g-1)
Coulombic efficiency (%)
Cycle number
anhydrous LiBr-LiCl
LiBr-LiCl monogydrate
c
Cell capacity (mAh g-1)
anhydrous LiBr-LiCl
LiBr-LiCl monogydrate
4:1
1:1
1:2
0.2 C
0.5 C
1 C
0.2 C
Cycle number
d
Output voltage (V)
Capacity (mAh g-1 total electrodes)
Wh kg-1
Non-aqueous
Aqueous
LBC-G/G
LiMn2O4/G
NCA/G
LCO/G
NCM622/G
LFP/G
LiCoO2|Li4Ti5O12
LiMn2O4|TiO2
LiMn2O4|Mo6S8
LiMn2O4|VO2
HV-LiCoO2|S
LiMn2O4|LiTi2(PO4)3